

High temperature finite-size effects in the magnetic properties of Ni nanowires

R. López-Ruiz,^{1,2} C. Magén,^{2,3} F. Luis,^{1,2} and J. Bartolomé^{1,2}

¹*Instituto de Ciencia de Materiales de Aragón (ICMA), C.S.I.C.-Universidad de Zaragoza, E-50009 Zaragoza, Spain*

²*Departamento de Física de la Materia Condensada, Universidad de Zaragoza, E-50009 Zaragoza, Spain*

³*Laboratorio de Microscopías Avanzadas (LMA), Instituto de Nanociencia de Aragón (INA)-ARAIID, Universidad de Zaragoza, E-50018 Zaragoza, Spain*

(Received 12 April 2012; accepted 9 August 2012; published online 2 October 2012)

The magnetic response of nickel nanowires embedded in porous alumina has been investigated in a wide temperature range, from 5 K up to 700 K. Hysteresis loops and magnetization isotherms were measured on samples of Ni nanowires with different sizes and morphologies up to the Curie temperature. At room temperature, the magnetic response shows evidences of a particle-to-wire crossover above an aspect ratio $L/D=4.3$. The magnetic coercivity of high aspect ratio Ni nanowires in the direction parallel to the nanowires has a maximum at $T\approx 400$ K, while in the parallel direction H_c decreases continuously with increasing temperature. It is explained in terms of competing anisotropies, magnetocrystalline and magnetoelastic. The expansion of the aluminium support of the membrane plays a fundamental role in the temperature dependence of the coercive field. We find also that T_C progressively decreases due to a finite-size effect as the wire's diameter decreases. © 2012 American Institute of Physics. [<http://dx.doi.org/10.1063/1.4756038>]

I. INTRODUCTION

Nanowires are materials of potential interest for applications as ultra high-density magnetic recording media,¹ electronic devices,² optics,³ or biological chip-based sensors.⁴ In addition, ordered arrays of ferromagnetic nanowires offer the opportunity to study magnetism at the mesoscopic scale.⁵ Nanowires can be produced by a template-assisted method⁶ using a porous alumina membrane (PAM). PAMs can be electrochemically produced by anodization of aluminium foil. The arrangement and shape of alumina pores are determined by the applied voltage, temperature, and type and concentration of the electrolyte.⁷ Thus, PAM can be used to produce large areas of periodic nanostructures in an economical way.

Motivated by their interesting properties and prospects of applications, an extensive experimental work has been done since Wernick *et al.*,⁸ for decorative purposes, gave color to anodized aluminium by introducing electro-chemically metallic nickel into the pores of the alumina protective film. Nanowires down to 10–20 nm in diameter can be prepared in PAM.⁹ Highly ordered metallic arrays may also be constructed by replication technique using PAM.¹⁰ Despite extensive work on the magnetic properties of transition metal nanowires,^{11–14} some questions remain open, namely the magnetic behavior of wires at early stages of growth, and how it depends on the aspect ratio ($m=L/D$) and the size-effects on fundamental magnetic parameters above room temperature like coercivity and ordering temperature.

In the present work, we first establish the aspect ratio m in a Ni filled PAM array that determines the crossover from a particle-like magnetic behavior, dominated by the intrinsic magnetic anisotropy, to a wire-like magnetic behavior, dominated by the shape and stress-induced anisotropies.

In a second step, we have also extended the determination of parallel and perpendicular coercivities of high aspect ratio Ni wires to a range of temperatures not covered until present, up to above the Curie temperature (T_C). Our study shows that these materials do not undergo superparamagnetic blocking as a function of temperature, which is typical of other particulate materials. This property can be relevant for applications like thermal recording.¹⁴

Finally, the variation of the ferromagnetic ordering Curie temperature T_C reveals the influence of finite-size effects. We observe a reduction in T_C with decreasing diameter, which can be associated to the fact that the spin-spin correlation length is cut-off by the wire boundaries, as predicted in Ref. 15.

II. EXPERIMENTAL DETAILS

A. Synthesis protocol

We have applied the anodization synthetic method detailed in the literature^{5,16,17} to prepare Ni nanowires inside a double-step anodized PAM.

Previously to the anodization, the aluminium foil was electropolished in order to eliminate the metallic centers present at the surface which come from the industrial aluminium foil production. These centers may introduce an extrinsic magnetic signal and need to be removed from the aluminium.

The synthesis of PAM consists of a thermally controlled current-forced oxidation of aluminium that is achieved by applying a constant voltage. Under acidic conditions, when $\text{pH} < 2.6$, alumina becomes partially soluble and the oxide film forms a porous structure.

The anodization process is made in two steps. In the first step, at fixed DC voltage V , the anodization proceeds till the

bottom of the pores arrange in a nearly hexagonal pattern, at local level. The alumina is then removed to let the aluminium, puckered with the pattern acting as template for the second anodization. Experimentally the time t_1 was determined by measuring the current vs. time and checking when it remains constant. It was found that $t_1 = 30$ min was sufficient in all cases. In the course of the subsequent second anodization, during the time t_2 , the regular pores are formed with a length proportional to t_2 . Times t_1 and t_2 were chosen to attain the “soft regime” preparation conditions defined in Ref. 17. The change of the electrolyte solution obeys to the need of preventing the strong fizzing and heat emission typical of the “hard regime.” At the end of the anodization process, the anodization voltage is gradually reduced to decrease the thickness of the barrier layer separating the Al and Al_2O_3 layer.¹⁸ In all cases, the anodization times were fixed to the values $t_1 = 30$ min and $t_2 = 120$ min. In these samples, with $t_2 = 120$ min, the pore length is expected to be around $3\text{ }\mu\text{m}$ (in the samples with the lowest growth rate [40 V and oxalic acid]). The parameters (temperature, electrolyte, voltage V , first and second anodization times t_1 and t_2 , respectively) are summarized in Table I.

The filling of the pores is carried out by electroplating, using an AC electric voltage $V_{AC} = 15$ V that oscillates at a frequency $\nu = 100$ Hz.¹⁹ The wires were grown on an exposed area of 0.4 cm^2 in the middle of an anodized aluminium disc of 2.2 cm in diameter. The aluminium/alumina specimen is used as the cathode whereas a lead sheet is used as the anode. The electrolyte consists of a $\text{NiSO}_4 \cdot 7\text{H}_2\text{O}$ (50 g/l), H_3BO_3 (25 g/l), and glycerin (20 g/l) solution (pH = 4.11 at 27.7°C). During the deposition time (t_{plate}), metallic nickel cations get reduced and deposited inside the pores and nanowires grow from bottom to top.

B. Microstructure characterization: Controlling the aspect ratio

In order to determine the influence that the different synthesis parameters, such as anodization voltage or t_{plate} , have on the morphology of the membranes and wires, a systematic analysis with scanning electron microscopy (SEM) and transmission electron microscopy (TEM) was performed.

Images of the top and bottom faces of the samples were obtained with a JEOL JMS-6400 SEM and a Hitachi H4300FE Field Emission SEM. Morphology, microstructure, and pore's length (L) and diameter (D) were studied with a FEI Titan TEM operated at 300 kV using bright field (BF) imaging, selected area electron diffraction (SAED), and high angle annular dark field (HAADF) scanning TEM (STEM). For this purpose, cross sectional TEM specimens were prepared. Con-

ventional mechanical (tripod) thinning and ion milling techniques were used to obtain specimens transparent to electrons.

We find that the alumina layer grows very uniformly over the surface of aluminium. The porous membrane shows a typical arrangement of nanopores close to honeycomb at local level (Fig. 1). It consists of an array of columns, each containing a pore at its center and separated from the aluminium metal by a scalloped spherical oxide barrier layer.²⁰ The columnar structure is clearly observed after removing the aluminium from the bottom of the plate (Fig. 1(b)).

From the SEM microscopy images, one concludes that each pore column has, on average, six adjacent columns, although the expected hexagonal periodicity of the spatial distribution of the nanopores is not complete in our samples. One can determine, on average, the average columnar cell (h-cell) parameter H , and the pore diameter D , both of which increase linearly with the anodization voltage V , as shown by Fig. 2. More specifically, we find $H = KV$, where $K = 2.5\text{ nm/V}$ and $D = kV$, where $k = 0.748\text{ nm/V}$. The k value we find differs from 1.2 nm/V reported in Ref. 5 possibly because the anodization temperatures in these two experiments were different. The minimum pore diameter achieved was $27 \pm 2\text{ nm}$ for $V = 40\text{ V}$ (see Fig. 2).

From the analysis of the PAM images, the porosity coefficient of the samples is found to be about 9%. Within the experimental uncertainties, these porosity values are in agreement with the 10% predicted in Ref. 17 for perfectly arranged pore arrays. The mean pore diameter, i.e., the wire diameter, has a confidence better than 5%. Reproducibility studies (not shown) reveal that the anodization time has no influence on the cell's or pore's diameter.

The analysis of TEM images provides information on the thickness of the alumina layer, which increases linearly with the anodization time t_2 , and on the filling of the pores, i.e., on the length of the nanowires and its distribution (see Fig. 3). The pores possess large aspect ratios ($L \gg D$), with lengths in the range of microns, and some nanometers in diameter. A list of the samples used in this work is given in Table II, which also includes the anodization voltages used to obtain them, the dimensions measured by SEM and TEM

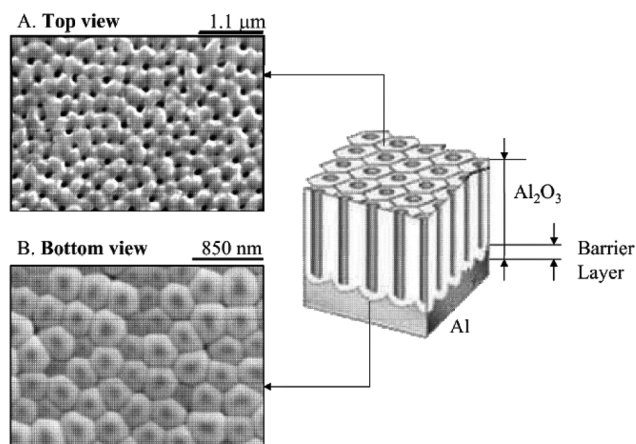


FIG. 1. Schematic drawing of the nanoporous alumina structure obtained as a result of the anodic oxidation of an Al foil. SEM images of the top (A) and the bottom (B) faces of a sample synthesized at 160 V during $t_2 = 120$ min in H_3PO_4 1%, from which the underlying Al layer has been removed.

TABLE I. Table of anodization conditions employed in the synthesis of the PAMS.

Electrolyte	Voltage range (V)	t_1 (min)	t_2 (min)	T ($^\circ\text{C}$)
H_2SO_4 (1M)	0–40	30	120	0
$\text{H}_2\text{C}_2\text{O}_4$ (0.3M)	40–80	30	120	0
H_3PO_4 (4%)	80–140	30	120	10
H_3PO_4 (1%)	140–180	30	120	10

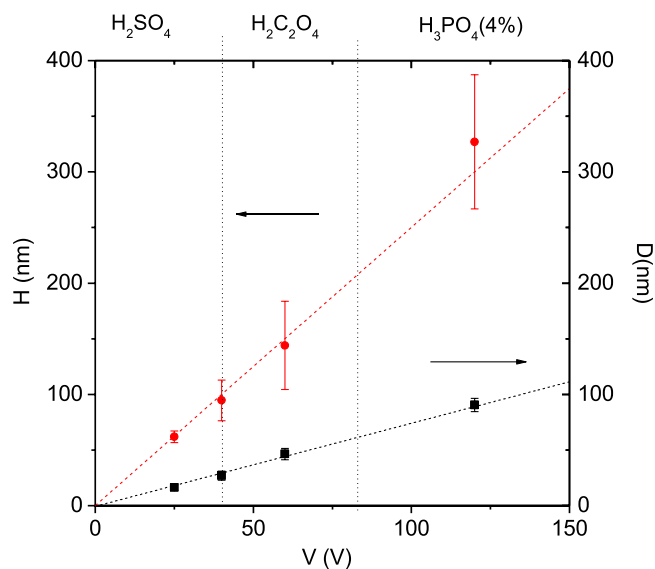


FIG. 2. Dependence of h-cell diagonal (H) and pore diameter (D) on the anodization voltage. Temperatures and electrolytes used are described in Table I and marked in the top scale. All samples were anodized twice, and the anodization times were $t_1 = 30$ min and $t_2 = 120$ min. Red and black dotted lines are linear fits for H and D , respectively. Bars indicate the distribution widths of these two parameters.

(average diameter D , average Length L), as well as the aspect ratio $m = L/D$.

As said in Sec. II A, the pore length is about $3 \mu\text{m}$ in the samples with the lowest growth rate. The filling fraction of

the pores can be calibrated by the plating time (t_{plate}). That is, a linear relation (growing rate of 10^2 nm per minute) is found between the average wire length and t_{plate} (Fig. 3(a)). For $t_{\text{plate}} > 30$ min there is overfilling of the holes and a continuous Ni overlayer is formed. Since the magnetic signal of the continuous nickel overlayer can easily shadow the contribution from the wires, the samples prepared for magnetic measurements PAMs were not filled for times longer than 10 min. Both the saturation magnetization M_s and the wire's length show a qualitatively similar increase with the t_{plate} , for any given average diameter, therefore, evidencing that the filling time increases the amount of nickel and directly determines the wire's length. The number of filled pores is about 1.3%; i.e., we have a weakly filled membrane with few pores filled.⁵ Although we know the average length and diameter of the nanowires in each sample, it was not possible to obtain a quantitative determination of M_s in emu per gram of Ni because the filling factor cannot be controlled, and therefore the Ni mass contained in a given sample cannot be determined with sufficient accuracy.

High-resolution cross section images of sample 8 show that the pores are filled with polycrystalline Ni (Fig. 4(a)). The diameter of the wires ($D = 27 \pm 2 \text{ nm}$) can be clearly determined from Fig. 4(b), that shows a magnification of a region near the surface of the alumina matrix. The typical branching at the bottom of the pore due to voltage reduction is also clearly observed. The average length of the branched portion of the pores and, as a consequence, of the nanowires

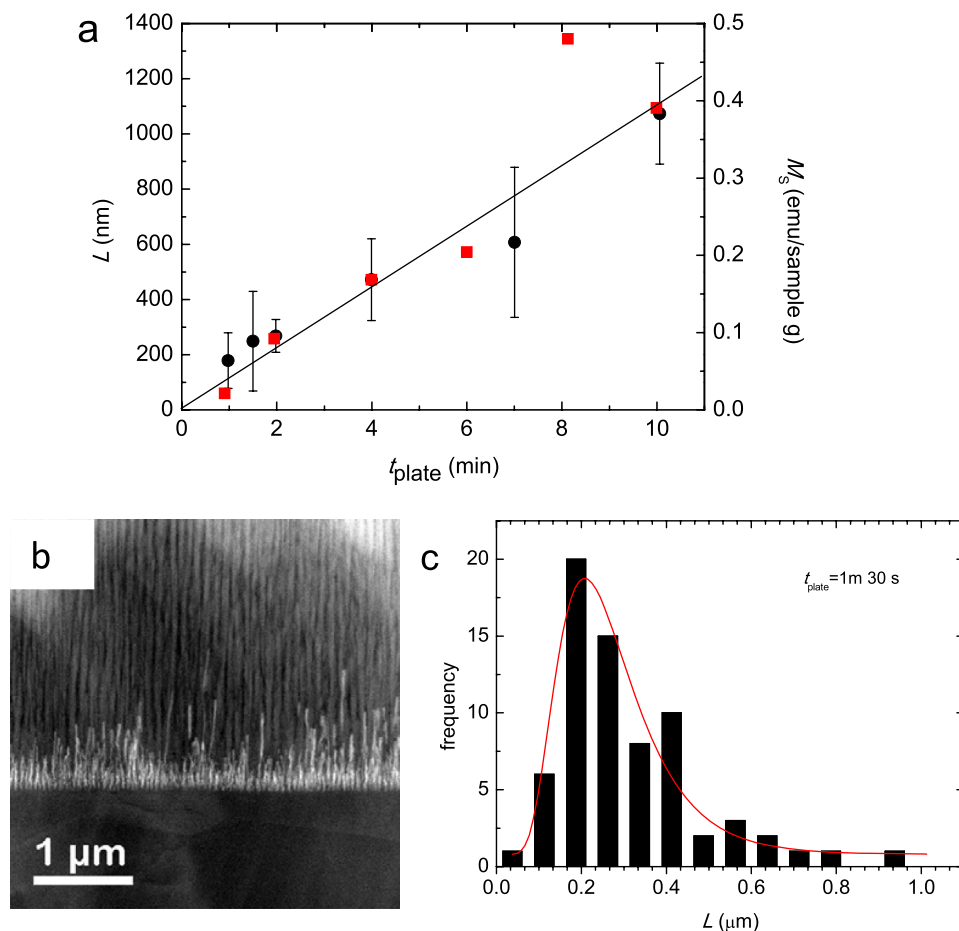


FIG. 3. (a) Dependence of the Ni wires' length (circles) and of the saturation magnetization obtained from hysteresis loops (squares) as a function of t_{plate} . (b) Cross-section BF TEM image of a sample with $t_{\text{plate}} = 1.5$ min. PAM were produced using an electric voltage $V = 40 \text{ V}$, $t_1 = 30$ min, and $t_2 = 120$ min. The plating voltage had an amplitude of $V_{AC} = 15 \text{ V}$ and a frequency $\nu = 100 \text{ Hz}$. (c) Wire's length frequencies for the same sample fitted to a lognormal distribution function.

TABLE II. Average diameter D , average length L , and aspect ratio $m = L/D$ of samples used in Sec. III. D: dendritic, NW: Nanowire.

Sample	Type	V (V)	D (nm)	L (nm)	m
1	D	25	16 ± 2	$\leq 30 \pm 5$	≈ 1
2	D & NW	40	27 ± 2	101 ± 50	3.7 ± 2.2
3	NW	40	27 ± 2	117 ± 50	4.3 ± 2.4
4	NW	40	27 ± 2	135 ± 70	5.0 ± 2.5
5	NW	40	27 ± 2	152 ± 70	5.6 ± 2.3
6	NW	40	27 ± 2	207 ± 100	7.6 ± 3.6
7	NW	40	27 ± 2	416 ± 100	15 ± 3.7
8	NW	40	27 ± 2	1100 ± 120	41 ± 10
9	NW	60	46 ± 3	1040 ± 120	23 ± 5
10	NW	120	90 ± 3	1100 ± 120	12 ± 2

is about 30–40 nm and the diameter of each branch reduces to about 10 nm. The polycrystalline character of the wire is proven by the SAED pattern shown in Fig. 4(c), where the multiple spots from the Ni fcc grains have been indexed accordingly. In Fig. 4(d), we show the amplified HAADF-STEM image of the dendritic zone at the bottom of the nanowires.

III. MAGNETIC BEHAVIOR

The presence of a macroscopic amount of nanowires oriented in a template enables us to obtain information on their magnetic properties from conventional macroscopic measurements. Hysteresis loops and magnetization isotherms were measured over a wide temperature region from 4 K up to above the Curie temperature. These measurements were performed using a commercial SQUID magnetometer.

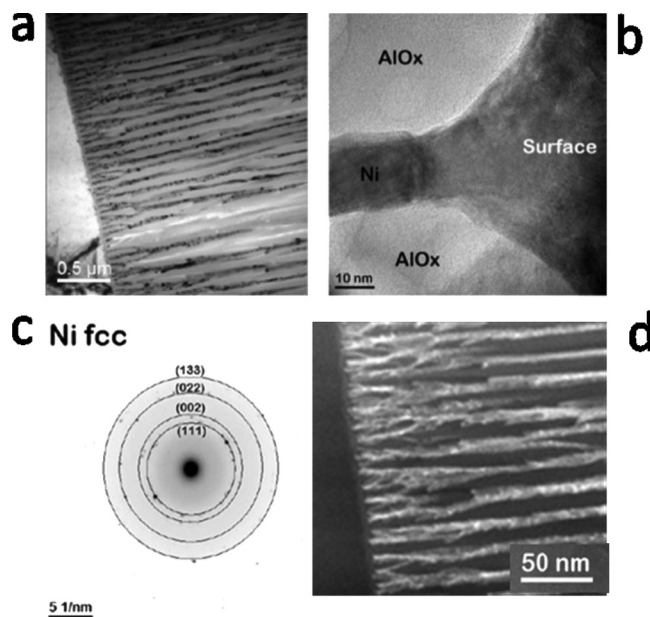


FIG. 4. (a) BF TEM image of a cross section specimen of a PAM with $t_{\text{plate}} = 30$ min (the pores are fully filled). PAM were produced using an electric voltage $V = 40$ V, $t_1 = 30$ min, and $t_2 = 120$ min. (b) BF TEM of the same sample at the matrix surface. (c) SAED pattern indexed according to the fcc Ni structure. The polycrystalline character of the nanowires is evidenced by the multiple spots. (d) HAADF-STEM amplification of the dendritic zone at the nanowires bottom.

A. Length influence: Particle-to-nanowire crossover

Figure 5 shows hysteresis loops measured at room temperature with the magnetic field applied parallel and perpendicular to the wires' axes on a sample with aspect ratio $m = L/D = 23 \pm 3$; i.e., for an array of long nanowires. The parallel loop shows larger values of remanence M_r and coercivity H_c , whereas the perpendicular magnetization is nearly fully reversible; i.e., it has a very small H_c . The squareness of the hysteresis loop is characteristic of inhomogeneously filled membranes, with very weak dipolar wire-wire interactions. In what follows dipolar interactions are, for this reason, considered as negligible.²¹ The anisotropy axis is parallel to the wire axis. Hysteresis is then observed only when the applied field has a large component along this axis whereas, by contrast, the magnetization rotates reversibly towards the magnetic field when the latter is perpendicular to the wire.

As the hysteretic behavior is dominantly caused by the shape anisotropy, the hysteresis loops are expected to depend on the wire's aspect ratio. Although the dependence of the magnetic behavior with the aspect ratio has been studied extensively for nickel nanowires, within the framework of a simple Stoner-Wohlfarth model,^{5,9,22,23} those studies were done on samples with particle's lengths long enough to magnetically behave as a wire, with a well-established shape anisotropy. Our study deals with smaller aspect ratios where the shape anisotropy competes with other sources of magnetic anisotropy, including the intrinsic magnetocrystalline anisotropy, with easy axes oriented at random (see Fig. 4) or effects arising from the wire branching near the alumina layer. Under these conditions, a deviation from the pure wire-like magnetic behavior is expected as the aspect ratio decreases. To achieve this study, samples of nanowires with a fixed diameter ($D = 27$ nm) and different lengths, tuned by t_{plate} , were prepared. The aspect ratio, given by the parameter $m = L/D$, was then increased for a fixed diameter.

In Fig. 6, we show the hysteresis curves for wires with $m = 3.7, 4.3$, and 7.6 . These values correspond, respectively, to the smallest aspect ratio investigated in the present work, to an intermediate value and to the aspect ratio above which the $M(H)$ curves become insensitive to m . One should bear in mind that the dendritic zone amounts to about 1/3, 1/4, and 1/5 of the nanowires length, respectively. The curves for

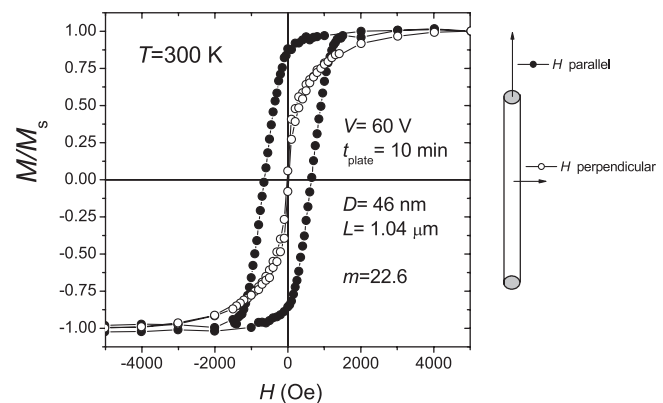


FIG. 5. Hysteresis loops measured at 300 K for fields applied parallel and perpendicular to the wire's axes of a sample with $D = 46$ nm and $L = 1.04$ μm.

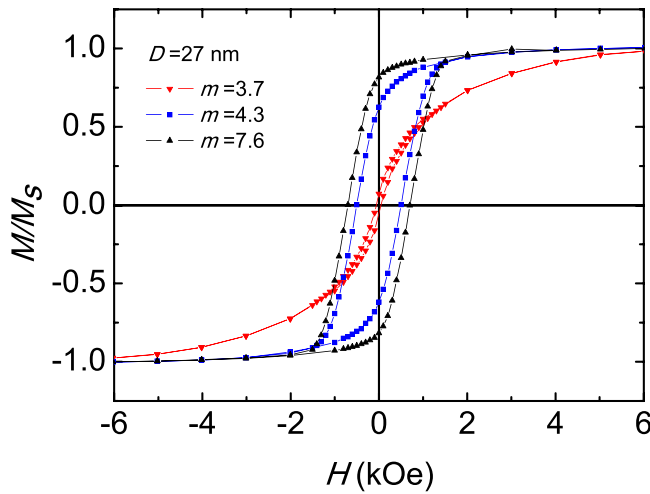


FIG. 6. Hysteresis loops (lines) measured with H along the wires direction, at $T = 300$ K, for samples with $D = 27$ nm, and increasing aspect ratio.

$m = 3.7$ show a very small H_c and a gradual approach towards saturation, in marked contrast with the close to square hysteresis expected for a long wire. For $m = 4.3$, both H_c and the squareness ratio M_r/M_s increase. Finally, samples with $m \geq 7.7$ show the largest H_c and hysteresis loops with a high squareness ratio typical of nanowires.

Figure 7 shows the dependence of M_r/M_s and H_c on the aspect ratio $m = L/D$. Both parameters follow the same qualitative behavior, rapidly increasing first and then tending to saturate as m increases. These results show that wires with aspect ratios $m < 4$ tend to behave as superparamagnetic nanoparticles.²⁴ It is worth mentioning here that the squareness ratio measured at $T = 300$ K tends to 0.8 for $m \gg 1$, and not to 1 as would be expected for a perfectly isolated magnetic cylinder. The reason is that the demagnetization field of the whole sample (not to be confused with the demagnetization field of each wire) tilts the square hysteresis curve by a slope inversely proportional to the demagnetization factor.⁵ In this respect, the use of rather dilute, i.e., non-perfectly filled, membranes is an advantage as it reduces the effects of magnetostatic or dipolar fields.²¹ Since the curves for small m do not accept a simple correction for the demagnetization effect, we have preferred to give in Figs. 6 and 7 the direct experimental results. One of

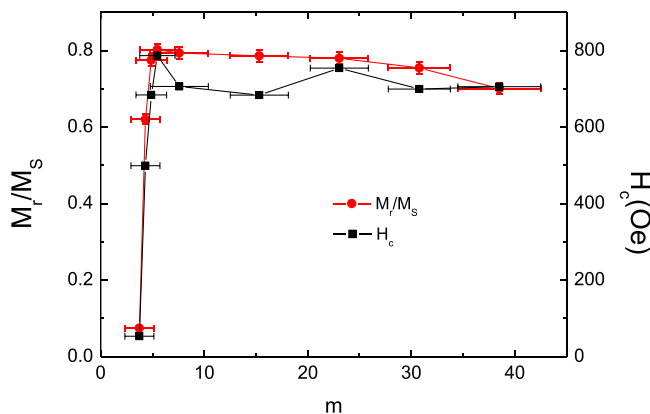


FIG. 7. Squareness ratio M_r/M_s and coercive field H_c as a function of aspect ratio m , measured with H parallel to the wires direction at $T = 300$ K, for samples with $D = 27$ nm.

the magnitudes studied is the ratio of remanence to saturation defined as the squareness of the loop M_r/M_s . It informs us of the particle to nanowire ratio in the magnetic response; as the squareness ratio decreases the superparamagnetic behavior is approached. The second is the coercive field since at $H = H_c$ the mean field produced by the average magnetization of the sample is zero and interactions with the mean field can be neglected.

Several physical mechanisms can contribute to the particle-to-wire crossover. The shape magnetic anisotropy decreases with decreasing m .²⁵ Indeed, the shape anisotropy field of a perfect magnetic cylinder is

$$H_A^{sh} = (N_{x,y} - N_z)M_s, \quad (1)$$

where N_z and N_x are the demagnetization factors for axes parallel and perpendicular to the long axis, respectively. It follows then that H_A must decrease with m , simply because the difference between $N_{x,y}$ and N_z also decreases. In real nanowires prepared inside alumina templates, this effect might be enhanced. For $m = 3.7$, the wire dendritic branches account for about 1/3 of the total wire's length. These branches have a lower magnetic texture, as can be seen from the TEM images in Fig. 4(d), thus, also a lower shape anisotropy than the central section of the wire.

For sufficiently low m , the shape anisotropy might eventually compete with the intrinsic magnetocrystalline anisotropy, which is characterized by a random orientation of the anisotropy axes. This competition between magnetic anisotropies with different textures has been observed in the case of Co nanowires, for which the very strong magnetocrystalline anisotropy dominates even in limit $m \rightarrow \infty$.⁵ For polycrystalline Ni, the anisotropy field H_A^M associated with the cubic magnetocrystalline anisotropy is $H_A^M = 0.64K_1/M_s \approx 10^3$ Oe, where $K_1 \approx 8 \times 10^5$ erg/cm³ is the anisotropy constant along the [100] axis.²⁶ This field can be compared to H_A^{sh} calculated with Eq. (1). For $m = 4.3$; i.e., close to the crossover (see Fig. 7), we find $H_A^{sh} = 2 \times 10^3$ Oe, which is of the same order of magnitude as H_A^M . Notice also that K_1 of nanometer sized grains can be enhanced with respect to the bulk anisotropy. Experiments performed on 4.2 nm Ni nanoparticles²⁶ give $K_1 \approx 12 \times 10^5$ erg/cm³, thus, $H_A^M \approx 2 \times 10^3$ Oe, in very good agreement with the expected H_A^{sh} at the crossover. Finite size effects would then shift the particle-to wire crossover to higher values of m . Also, thermally activated magnetic relaxation becomes faster as the magnetic volume is reduced, thus, further contributing to reduce both M_r and H_c . Relaxation phenomena are certainly important in wires with $m = 3.7$, as they show close to zero remanence and coercivity, that is, almost no magnetic memory. As we discuss in the Sec. III C below, the magnetic coercivity becomes much more robust against thermal fluctuation in the case of sufficiently long nanowires.

B. Temperature dependence of H_c

Figure 8 shows the temperature dependence of the coercive field when the field is applied parallel and perpendicular to the nanowires direction. Let us first consider the region below room temperature. Contrary to some previous

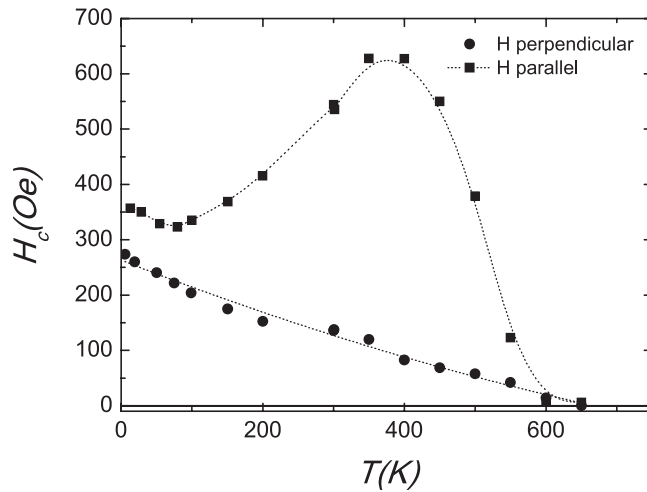


FIG. 8. Dependence of the coercive field on temperature for a sample synthesized with dimensions $L = 1100$ nm and $D = 27$ nm. Measurements were performed for fields applied parallel (■) and perpendicular (●) to the wires' axes. The lines are guides to the eye.

experimental studies in Refs. 5 and 27, we find that for H parallel to the nanowires H_c decreases when T decreases, showing a minimum at a finite $T \approx 90$ K.

In contrast, when the magnetic field is applied perpendicular to the wires' axis, a monotonic increase of H_c with cooling is observed. This behavior can be associated with the appearance of a new perpendicular anisotropy that competes with the axial one dictated by the shape anisotropy.

Since the magnetocrystalline anisotropy can be neglected due to its weakness and to the polycrystalline character of the Ni deposited inside the pores (see Sec. II B), the anomalous dependence of H_c on temperature must be associated with extrinsic effects. A similar behaviour has been found in Refs. 12, 13, and 27, and has been ascribed to a thermally-induced magnetoelastic effect. As the thermal expansion coefficients (α) for aluminium $\alpha(\text{Al}) = 23.8 \times 10^{-6} \text{ K}^{-1}$, nickel $\alpha(\text{Ni}) = 13 \times 10^{-6} \text{ K}^{-1}$ and alumina $\alpha(\text{Al}_2\text{O}_3) = 6 \times 10^{-6} \text{ K}^{-1}$ are rather different, a decrease in temperature produces a compressive stress on the wires. The positive values of α indicate that materials compress with decreasing temperature. As the thickness of the aluminium substrate is very large ($\sim 100 \mu\text{m}$) with respect to that of the alumina matrix ($\sim 3 \mu\text{m}$), the aluminium foil exceeds the force exerted by the matrix and cannot be neglected in the analysis.¹³ Alternative interpretations^{12,27} that neglect the effect of aluminium would in fact give rise to just the opposite dependence of H_c with temperature.

Since the energy associated with a directional exerted stress reads $E_\sigma = K_\sigma \cos^2 \theta$, where θ is the angle between the exerted stress and magnetization, and K_σ , the magnetoelastic constant has a positive value, the magnetoelastic effect tends to orient spins perpendicular to the wire axis in competition with the shape anisotropy.¹³ We have estimated, in our case, that $K_\sigma = 9.9 \times 10^5 \text{ erg/cm}^3$, considering that the Ni magnetostrictive constant $\lambda_s = -3.4 \times 10^{-5}$, and that the external stress along the wire $\sigma = 19.5 \times 10^8 \text{ Nm}^2$. The resulting K_σ value is larger than the magnetocrystalline $K_M = 1.50 \times 10^5 \text{ erg/cm}^3$, and shape anisotropy for this sample $K_{\text{sh}} = 7.3 \times 10^5 \text{ erg/cm}^3$,

and becomes predominant at low temperatures. As a result, magnetoelastic effects will turn progressively the net anisotropy axis towards the perpendicular direction as temperature decreases. This naturally explains both the decrease of the H_c when the field is applied parallel to the wire's axis, and a concomitant increase of H_c when the field is applied perpendicular to it. As nickel is assumed to be intimately linked with the alumina matrix, the alumina contraction and the reduction of the pores is only controlled by the aluminium contraction during the cooling, resulting in a lateral stress on the wires that gives rise to an axial expansion. As a consequence, the perpendicular anisotropy increases, and since this contribution compensates the axial shape anisotropy, the net effect is a reduction of H_c as temperature decreases.

If aluminium is neglected in this analysis, when temperature decreases the alumina would exert a tensile stress on the wires that tends to orient the spins along the wire, i.e., just the opposite effect and contrary to the observed magnetic phenomenology. In fact, in Ref. 5, where the aluminium was removed from the sample before the magnetic measurements were done, the coercive field increases monotonically with decreasing T by the effect of the suppression of the thermally activated magnetic relaxation. Our results, complemented with those in Ref. 5, confirm that the thermally-induced magnetoelastic effect is due to the supporting aluminium sheet, as discussed in Ref. 13.

Above room temperature, in a range of temperatures not covered until now, we have observed that H_c , measured with the field applied along the wire's direction, first increases, then has a maximum at about 400 K, and finally decreases monotonically up to the Curie temperature T_C . In contrast, when the field is applied perpendicular to the wires, H_c decreases monotonically till it disappears at T_C . To explain this feature, two opposite effects of increasing temperature above room temperature, which both affect H_c , have to be considered, namely magnetoelastic and shape anisotropy.

Above 300 K and up to T_C one should take into account the temperature dependence of: (a) the Ni magnetostriction coefficient λ_s that remains negative at all temperatures, while its modulus decreases very steeply and becomes zero at T_C ,^{28,29} and (b) the shape anisotropy constant K_{sh} that depends on M_s^2 (Eq. (1)), thus, it decreases strongly with increasing T , just as M_s does, and tends to zero as the Curie temperature is approached.

With the same arguments as in the previous paragraphs, as T increases, the aluminium sheet tends to expand the nickel wire sideways (oppositely to what happens when temperature is reduced) resulting in an external tensile stress that would lead to an axial contraction. Therefore, when T increases the magnetoelastic effect would enhance the net anisotropy along the wire, till the temperature is reached when K_σ decreases because of the decrease in $|\lambda_\sigma|$ invoked above. This explains the maximum in H_c observed at 400 K. Above this temperature, the easy anisotropy axis remains along the wire's direction, and both the magnetoelastic and the shape anisotropy cooperate in decreasing H_c till its disappearance at T_C .

In the perpendicular direction, H_c is reduced continuously as T increases, since in that direction there is just one component giving rise to perpendicular anisotropy.

C. Size dependent Curie temperature

In order to determine the Curie temperature, temperature dependent magnetization measurements were performed at fixed field values. For temperature calibration purposes, a Ni bulk sample was measured as well, yielding the Curie temperature $T_C = 633$ K,³⁰ which is taken as reference below. An important advantage of our preparation method is that the nickel nanowires are protected from oxidation and structural damage at elevated temperatures.

As we can see in Fig. 9, a well defined phase transition between a ferromagnetic and a paramagnetic phase is observed. The measurements were performed while heating from 300 to 650 K and cooling back to 300 K. The Curie temperature was determined as the intersection between linear fits of M in the ordered and paramagnetic regions (an example is shown in the inset of Fig. 9). The magnetization curve was fully reversible, yielding the same Curie temperature in both runs. This lack of irreversibility in the magnetization allows us to state that impurities, recrystallization, diffusion of oxygen, reaction with the lattice, or other suspected perturbations of the sample are not present in our nanowires.

The ferromagnetic behavior below the Curie temperature was confirmed by hysteresis loop measurements. As hysteresis is present in all the ferromagnetic range and only disappears above the Curie temperature, the superparamagnetic blocking is not present in these samples. This means that the anisotropy barrier energy $\Delta E = K_{eff}V$, where K_{eff} is the effective (shape + stress) anisotropy constant, remains sufficiently high to keep a time average remanence also at elevated temperatures. This phenomenon might be of interest for applications in perpendicular magnetic media and thermally assisted recording. In particular, replicas with the information fixed on the magnetization of the wires can be recorded simply by first heating and then subsequently cooling a replica sample while it is in contact over an original one.¹⁰ Note that $M(T)$ curves for fields applied parallel and perpendicular show different values. This is because a field of 1000 Oe is not able to produce a full saturation of the

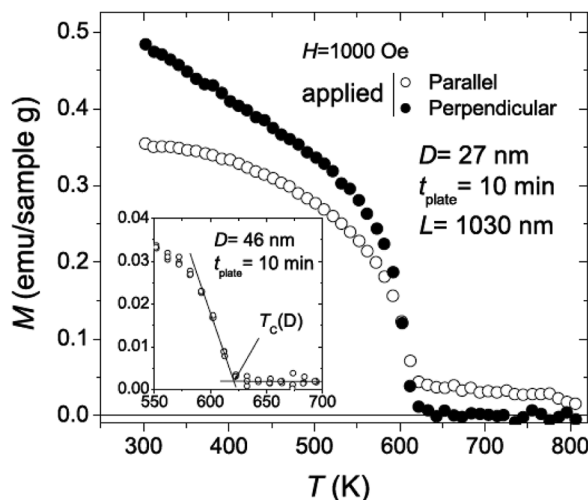


FIG. 9. Temperature dependence of the magnetization of a sample with $D = 27$ nm and $L = 1030$ nm. The inset illustrates the procedure followed to determine the Curie temperature for a sample with $D = 46$ nm and $L = 1030$ nm.

magnetization (see Fig. 9), i.e., the anisotropy remains high up to nearly T_C .

To study the dependence of the Curie temperature T_C on the average diameter, samples with $L \approx 1000$ nm and $D = 16, 27, 46$, and 90 nm average diameter were measured. As is shown in Fig. 10, although T_C of the sample with $D = 90$ nm is identical to that of the Ni bulk, T_C decreases as the mean wire diameter is reduced. The reduction in T_C is already noticed for the sample with $D = 46$ nm diameter and amounts to 10 K for $D = 16$ nm. These results may be compared to those obtained for Ni nanowires grown in stress-free conditions.³¹ They found a qualitatively similar, although quantitatively stronger, reduction of T_C with decreasing diameter.

The reduction of the Curie temperature has been explained as due to finite-size effects, and was predicted theoretically in Ref. 15. As T approaches T_C , the correlation length $\xi(T)$ of a magnetic system increases according to a power law³²

$$\xi(T) = \xi_0 \left| 1 - \frac{T}{T_C(\infty)} \right|^{-\nu}, \quad (2)$$

where ξ_0 is the corresponding length extrapolated to $T = 0$, $T_C(\infty)$ is the bulk critical temperature and ν is a critical exponent. In systems with reduced dimensions (as a nanowire with diameter D), the growth of ξ with temperature is constrained by D , resulting in a reduction of the Curie temperature given by

$$\frac{T_C(\infty) - T_C(D)}{T_C(\infty)} = \left(\frac{\xi_0}{D} \right)^\lambda, \quad (3)$$

where $T_C(D)$ is the Curie temperature for a nanowire with diameter D and $\lambda = 1/\nu$.

From the fit of Eq. (3) to the data, shown in Fig. 10, we obtain a correlation length $\xi_0 = 1.7 \pm 0.5$ nm and a critical

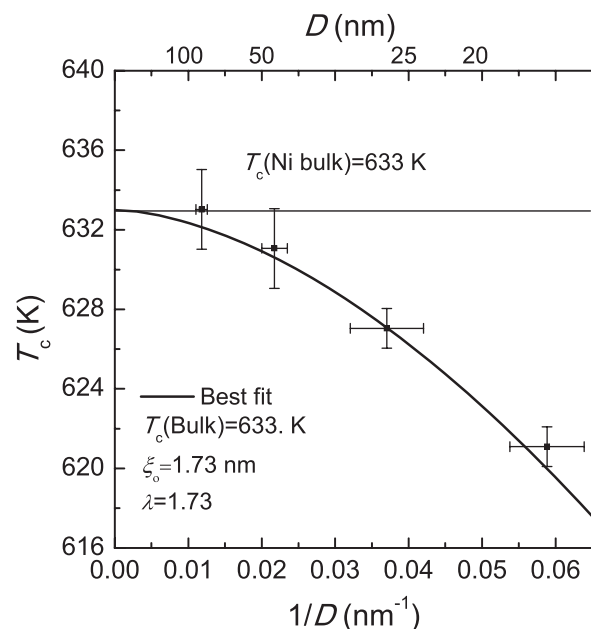


FIG. 10. Dependence of the Curie temperature on the wire's diameter, and as a function of $1/D$. The black thick line shows the best fit to data according to Eq. (3).

exponent $\lambda = 1.3 \pm 0.2$. The correlation length is longer than that of the unit cell, as is expected for a ferromagnet.

The correlation length and critical exponent on free standing Ni nanowires grown in mica, where the wires are free from stress,³¹ were found to be $\xi_0 = 0.8 \text{ nm}$ $\lambda = 0.94$. As in our case on Ni wires embedded in an alumina matrix, those samples do not show any reduction of the $T_C(D \rightarrow \infty)$ limit. However, the T_C reduction as a function of decreasing diameter found in the mica grown Ni nanowires is much stronger than that found in the present alumina template grown Ni nanowires. Since in both cases the stress from the matrix plays no role at these temperatures, it must be concluded that the difference is probably due to the different morphology of the grains in the polycrystalline Ni nanowires, that will play a role in the cut off correlation length. Our results are close to the predictions for a 3D Heisenberg ferromagnet ($\lambda = 1.4$), with only nearest neighbor interactions. The absence of a shift of $T_C(D \rightarrow \infty)$ with respect to T_C of the bulk implies that the observed reduction is basically a size-effect due to the cut-off of the correlation length sideways by the reduced wire diameter and the morphology of the grains in the nanowire.

IV. SUMMARY AND CONCLUSIONS

Controlling different parameters of the synthesis, such as the anodization voltage, or the anodization and plating times, Ni nanowires with well defined size, length and morphology were synthesized. The magnetic response of wires with different aspect ratios show evidences for a particle-to-wire crossover above a finite aspect ratio $m = L/D = 4.3$. Below room temperature, the compression stress, due to the different thermal expansion coefficients of aluminium and nickel, gives rise to a thermally induced magnetoelastic effect that reduces the coercivity as temperature is decreased. The latter behavior is shown only when aluminium is not removed from the samples. Besides, as temperature is increased above room temperature, the coercivity in the parallel directions shows a maximum at 400 K due to compensation of the increasing axial anisotropy caused by the aluminium expansion effect on the Ni wire (contraction along the axis), on one hand, and the anisotropy decrease due to the shape anisotropy decrease with M_s^2 , on the other hand.

The variation of magnetization with temperature for $m > 4$ does not show any evidence of a superparamagnetic blocking, which confers to this material a potential application in data storage and thermal recording. The Curie temperature progressively decreases with decreasing wire diameter. This reduction of the Curie temperature is attributed to finite-size effects and is consistent with theoretical predictions for the Curie temperature reduction due to the cut-off of the correlation length by the lateral dimensions of each nanowire. The Curie temperature of $D = 90 \text{ nm}$ nanowires agrees with that of bulk Ni. Therefore, there is no shift of $T_C(D \rightarrow \infty)$ with respect of the bulk value. This implies that stresses play no role in the decrease of T_C with decreasing diameter. These results are similar to the observed reduc-

tion of T_C in Ni nanowires embedded in mica, where stresses are very weak.³¹

ACKNOWLEDGMENTS

This work was partly funded under grants MAT2011/23791 (ORBIMAT) and MAT2009/13977-C03-01 (MOLCHIP), CONSOLIDER Project INGENIO 2010, from Spanish MICINN, and DGA E34 and E98 Projects.

- ¹R. L. White, *J. Magn. Magn. Mater.* **209**, 1 (2000).
- ²F. Capasso and S. Datta, *Phys. Today* **43**, 74 (1990).
- ³R. Agarwal and C. M. Lieber, *Appl. Phys. A: Mater. Sci. Proc.* **85**, 209 (2006).
- ⁴V. Patolsky, G. Zheng, and C. M. Lieber, *Nat. Protoc.* **1**, 1711 (2006).
- ⁵P. M. Paulus, F. Luis, M. Kröll, G. Schmid, and L. J. de Jongh, *J. Magn. Magn. Mater.* **224**, 180 (2001).
- ⁶H. He and N. J. Tao, *Encyclopedia of Nanoscience and Nanotechnology*, edited by H. S. Nalwa (American Scientific Publishers, Valencia, USA, 2004), Vol. 2, p. 755.
- ⁷S. Ono, M. Saito, M. Ishiguro, and H. Asoh, *J. Electrochem. Soc.* **151**, B473 (2004).
- ⁸S. Wernick, R. Pinner, and P. G. Sheasby, *The Surface Treatment and Finishing of Aluminum and Its Alloys*, 5th ed. (ASM International, Metals Park, OH, 1987), Vol. 1.
- ⁹M. Zheng, L. Menon, H. Zeng, Y. Liu, S. Bandyopadhyay, R. D. Kirby, and D. J. Sellmyer, *Phys. Rev. B* **62**, 12282 (2000).
- ¹⁰H. Masuda and K. Fukuda, *Science* **268**, 1466 (1995).
- ¹¹H. Zeng, R. Skomski, L. Menon, Y. Liu, S. Bandyopadhyay, and D. J. Sellmyer, *Phys. Rev. B* **65**, 134426 (2002).
- ¹²M. Vázquez, K. Pirota, J. Torrejón, D. Navas, and M. Hernández-Vélez, *J. Magn. Magn. Mater.* **294**, 174 (2005).
- ¹³A. Kumar, S. Fähler, H. Schlörb, K. Leistner, and L. Schultz, *Phys. Rev. B* **73**, 064421 (2006).
- ¹⁴K. Matsumoto, A. Inomata, and S.-y. Hasegawa, *Fujitsu Sci. Tech. J.* **42**, 158 (2006).
- ¹⁵D. P. Landau, *Phys. Rev. B* **14**, 255 (1976).
- ¹⁶H. Zeng, M. Zheng, R. Skomski, D. J. Sellmyer, Y. Liu, L. Menon, and S. Bandyopadhyay, *J. Appl. Phys.* **87**, 4718 (2000).
- ¹⁷K. Nielsch, J. Choi, K. Schwirn, R. B. Wehrspohn, and U. Gösele, *Nano Lett.* **2**, 677 (2002).
- ¹⁸R. C. Fumeaux, W. R. Rigby, and A. P. Davidson, *Nature* **337**, 147 (1989).
- ¹⁹A. L. Friedman and L. Menon, *J. Electrochem. Soc.* **154**, E68 (2007).
- ²⁰F. Keller, M. S. Hunter, and D. L. Robinson, *J. Electrochem. Soc.* **100**, 411 (1953).
- ²¹T. G. Sorop, K. Nielsch, P. Göring, M. Kroll, W. Blau, R. B. Wehrspohn, U. Gösele, and L. J. de Jongh, *J. Magn. Magn. Mater.* **272**, 1656 (2004).
- ²²D. AlMawlawi, N. Coombs, and M. Moskovits, *J. Appl. Phys.* **70**, 4421 (1991).
- ²³M. Vázquez, K. Pirota, M. Hernández-Vélez, V. M. Prida, D. Navas, R. Sanz, F. Batallán, and J. Velázquez, *J. Appl. Phys.* **95**, 6642 (2004).
- ²⁴J. L. Dormann, D. Fiorani, and E. Tronc, in *Advanced Chemical Physics*, edited by I. Prigogine and S. A. Rice (Wiley, New York, 1997), Vol. XCVIII.
- ²⁵E. du Trémolet de Lacheisserie, D. Gignoux, and M. Schlenker, *Magnetism* (Springer, 2003), Vol. 1, p. 37.
- ²⁶A. H. Morrish, *The Physical Principles of Magnetism* (John Wiley and Sons, New York, 1965).
- ²⁷H. Zeng, S. Michalski, R. D. Kirby, D. J. Sellmyer, L. Menon, and S. Bandyopadhyay, *J. Phys.: Condens. Matter* **14**, 715 (2002).
- ²⁸E. de Lacheisserie du Tremolet, *Phys. Status Solidi B* **54**, K135 (1972).
- ²⁹R. O'Handley, *Modern Magnetic Materials: Principles and Applications* (John Wiley & Sons, New York, 2000).
- ³⁰J. Sesé, J. Bartolomé, and C. Rillo, *Rev. Sci. Instrum.* **78**, 046101 (2007).
- ³¹L. Sun, P. C. Searson, and C. L. Chien, *Phys. Rev. B* **61**, R6463 (2000).
- ³²H. E. Stanley, *Introduction to Phase Transitions and Critical Phenomena* (Oxford University Press, Oxford, 1971).